

Investigation on multi-physical field simulations of blade ECM using vertical flow

Mingzhu Ren

Dong Zhu (✉ zhudong@nuaa.edu.cn)

Nanjing University of Aeronautics and Astronautics

Zhenhao Hou

Gaopan Lei

Research Article

Keywords: Electrochemical machining, Blade, Vertical flow, Bubble, Simulation

Posted Date: May 18th, 2022

DOI: <https://doi.org/10.21203/rs.3.rs-1635526/v1>

License:  This work is licensed under a Creative Commons Attribution 4.0 International License.

[Read Full License](#)

Investigation on multi-physical field simulations of blade ECM using vertical flow

Mingzhu Ren, Dong Zhu*, Zhenhao Hou, Gaopan Lei

College of Mechanical and Electrical Engineering, Nanjing University of Aeronautics and Astronautics, 29 Yudao Street, Nanjing 210016, China

*Corresponding author.

E-mail address: zhudong@nuaa.edu.cn.

Abstract

Electrochemical machining (ECM), an advanced manufacturing technology, is widely used in aero-engine blade machining. In blade ECM, the electrolyte flows through the inter-electrode gap, generating hydrogen bubbles and heat, which affect the conductance and thus influence the machining quality. This paper focused on the effect of bubble movement on the flow field and the machining quality of ECM. A novel vertical flow mode of electrolyte was proposed according to the bubbles dynamics analysis. Multi-physical field simulations of blade ECM using vertical and horizontal flows were carried out. With an initial gas void fraction and temperature at the inlet of 0 and 302.65 K, respectively, in both flow modes, the vertical flow reduced the gas void fraction and temperature at the outlet by 2.4% and 0.6 K, and increased the conductance by 0.47 S/m. Thus, the vertical flow of the electrolyte was beneficial in reducing the gas void fraction and controlling the temperature rise, while enhancing the conductance. Then, the corresponding experiments using a vertical flow were carried out. The machining deviation was found to range from 3.4 μm to 75.6 μm and surface roughness values of $Ra < 0.35 \mu\text{m}$. The machining quality was high and the variation observed in the experiments was consistent with the simulation results, the validity and correctness of the simulations were verified. Thus, the vertical flow mode proposed in this paper was appropriate, can be used for other complex structures in ECM.

Keywords: Electrochemical machining, Blade, Vertical flow, Bubble, Simulation

1. Introduction

As one of the key components of aero-engines, the mechanical properties and machining accuracy of the blades play an important role in the overall performance of the engine. Blades are generally made

of hard-to-machine metal materials with complex surfaces[1,2]. Compared with traditional machining methods, electrochemical machining (ECM) is widely used in aero-engine blade machining because of its excellent surface quality, absence of tool loss, and high machining efficiency [3-7]. However, as an electrochemical anodic dissolution process, ECM is a multiphysics coupling process, which involves flow field, electric field, thermal field, etc [8,9]. To determine the machining quality of ECM, many different physical disciplines and aspects need to be considered [10].

Then, there have been many studies on the multi-physical fields present in ECM, and various theoretical models have analyzed the coupling effects of these multi-physical fields. Kozak et al. [11] established relevant mathematical and theoretical models for simulating and predicting the shaping of ECM blades. A multi-physical model built by Fujisawa et al. [12] showed that the flow field characteristics were greatly affected by the Joule heat and bubble generation. Klocke et al. [13,14] established an interdisciplinary model and simulated the blade ECM process considering the electric field, flow field, and heat transfer.

In order to achieve high machining quality in ECM, a lot of researches have been carried out. Fang et al. established a multi-physical field coupling model to analyze the influence of a pulsating electrolyte flow on the machining accuracy[15]. The flow distributions along the machining gap with different electrolyte patterns were compared numerically and experimentally by Wang et al. [16]. The lateral flow mode was adopted in electrochemical trepanning (ECTr) to improve the uniformity of the flow field by Lei et al. **Error! Reference source not found.** To solve the problem of flow field stability, the cathode structure was optimized by Tang et al.[17] Guo et al. used a new blade flow mode to improve flow field uniformity [18]. Zhu et al. optimized the distribution of the flow field by adjusting the turning profile on the cathode [19]. However, little work has been done so far on the effect of bubble movement on the flow field and the machining quality of ECM.

In this study, considering the influence of gravity on bubbles, a novel vertical flow mode of electrolyte was proposed according to the bubbles dynamics analysis. A multi-physical model was developed to consider the electric field, fluid flow, reactant transport, and temperature, enabling the variations in the gas void fraction and temperature along the flow direction to be studied and the conductance to be analyzed. The simulation of horizontal flow was used for comparison with vertical flow. Moreover, experiments were carried out to analyze the influence of a vertical electrolyte flow on the machining accuracy and surface quality, and the validity of the simulation results was verified.

2. Bubble dynamics of blade ECM using vertical flow

In blade ECM, there are generally two flow modes in blade ECM, namely the lateral flow mode and the axial flow mode. Hydrogen and sludge are generated in the machining gap, and Joule heat is produced because of the current heating effect.

2.1 Electrolyte flow method

In the lateral flow mode, the electrolyte flows from the leading edge to the trailing edge[5], providing a short flow path to facilitate the discharge of by-products. However, this flow mode suffers from disordered flow at the inlet and uneven flow in the convex and concave channels of the blade (Fig. 1). In the axial flow mode, the electrolyte usually flows horizontally from root to tip, and the electrolyte is supplied separately to the channels of the convex and concave parts, allowing the flow rates in the two channels to be controlled [20]. However, because the bubbles generated by ECM accumulate along the flow direction, a high bubble rate occurs at the outlet. Thus, the machining gap gradually decreases from the inlet to the outlet, and the machining deviation becomes large at the outlet (Fig. 2(a)). To overcome the shortcomings of the current flow modes, a vertical flow mode is proposed in which the electrolyte flows vertically upwards from root to tip. Under the influence of gravity, the bubbles in vertical flow have different dynamics from those in horizontal flow, with an increased bubble velocity and reduced bubble rate.

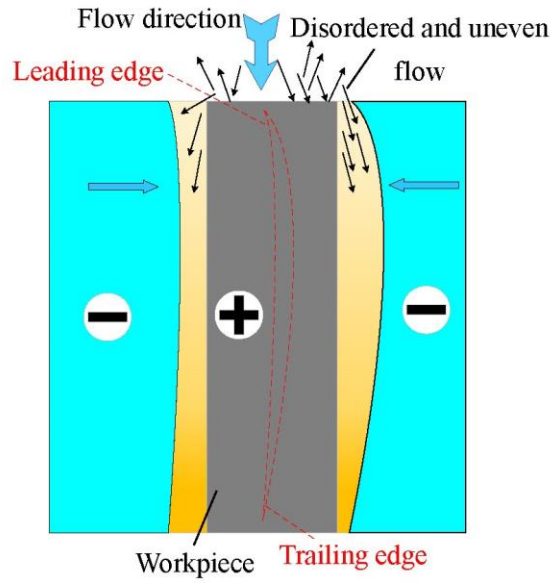


Fig. 1 Disadvantages of lateral flow. [20]

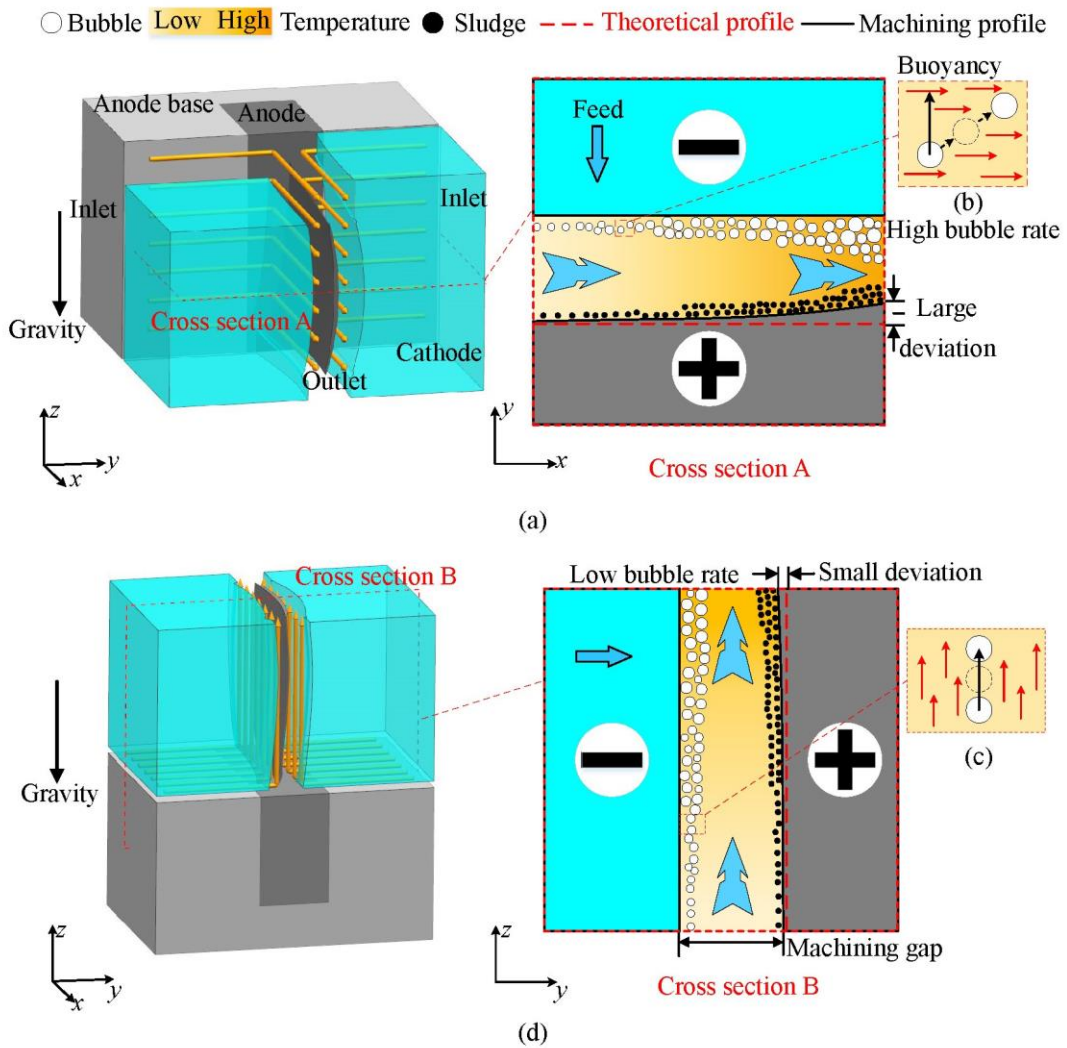


Fig. 2 Diagram of blade ECM in the axial flow mode: (a) horizontal flow, (b) diagram of buoyancy in

horizontal flow, (c) diagram of buoyancy in vertical flow, (d) vertical flow.

The buoyancy generated by the gravity gradient acts vertically upward; In horizontal flow, the direction of buoyancy is perpendicular to the direction of electrolyte flow, and so the bubble motion is affected (Fig. 2(b)). In vertical flow, the direction of buoyancy is consistent with the flow direction (Fig. 2(c)). As the density of the electrolyte is 1146 g/L, which is about 10^4 times that of the gas (0.089 g/L), the buoyancy significantly increases the bubble velocity and reduces the bubble rate in vertical flow. Hence, the bubble rate is low and the uniformity of conductance can be improved. As a result, the machining deviation is small at the outlet (Fig. 2(d)), and so better machining accuracy can be achieved in blade ECM using vertical flow. The specific dynamics of the bubbles are analyzed in the next section.

2.2 Bubble dynamics analysis

For a gas–liquid bubble column operating in the homogeneous regime, it can be assumed that the total force acting on a non-deformable spherical bubble moving in an unsteady, non-uniform liquid fluid is composed of separate and uncoupled contributions from the pressure gradient, drag, virtual or added mass, vorticity, and gravity [21]. The total forces on the bubbles in horizontal flow and vertical flow are shown in Fig. 4. To simplify the model, only the drag force \mathbf{F}_D , (i.e., the resistance exerted by the fluid), pressure gradient \mathbf{F}_P , and gravity \mathbf{F}_G are considered for the total force of the bubble.

$$\mathbf{F}_{total} = \mathbf{F}_D + \mathbf{F}_P + \mathbf{F}_G \quad (1)$$

The acceleration of the bubble can be obtained from the following equation:

$$m_b \frac{dv_g}{dt} = \mathbf{F}_{total} \quad (2)$$

where m_b is the mass of a single bubble and \mathbf{v}_g is the bubble velocity.

The resulting velocity of the bubble can be calculated by a simple formula [22]:

$$\mathbf{v}_{g_{m+1}} = \mathbf{v}_{g_m} + \left(\frac{dv_g}{dt}\right)_{m+1} DT \quad (3)$$

This states that the new bubble velocity is equal to the sum of the previous bubble velocity and the

current acceleration of the bubble multiplied by the time step DT .

The drag force \mathbf{F}_D acting on a suspended sphere, the direction of which is consistent with the flow direction of the electrolyte [23], is given as follows:

$$\mathbf{F}_D = -\frac{1}{2}C_D\rho_l\pi R_b^2|\mathbf{v}_l - \mathbf{v}_g|(\mathbf{v}_g - \mathbf{v}_l) \quad (4)$$

where \mathbf{v}_l , \mathbf{v}_g are the electrolyte and bubble velocities, respectively, and C_D is the drag coefficient.

For rigid spheres, this coefficient is usually approximated by the standard drag curve [24]:

$$C_D = \begin{cases} Re < 1000 \Rightarrow \frac{24}{Re}(1 + 0.15Re^{0.687}) \\ Re \geq 1000 \Rightarrow 0.44 \end{cases} \quad (5)$$

As the electrolyte is a contaminated system, the bubbles behave more like rigid particles [21]. Therefore, for turbulent flow with $Re > 1000$, the value of C_D is 0.44. ρ_l is the density of the electrolyte and R_b is the diameter of a single bubble.

The distributions of the pressure gradient in vertical and horizontal flows are shown in Fig. 3(a) and Fig. 3(b). Two units composed of the two gas-liquid phases are taken in the different flows to analyze the pressure gradient force \mathbf{F}_P acting on a single bubble. This can be calculated by the following equation:

$$\mathbf{F}_P = -V_b\nabla P \quad (6)$$

where V_b is the volume of a single bubble and ∇P is the pressure gradient of the electrolyte. To simplify the calculation, \mathbf{F}_P can be decomposed into two components, \mathbf{F}_{P_G} and \mathbf{F}_{P_D} , and which are derived from the gravity pressure gradient ∇P_G and the pressure drop ∇P_D due to fluid velocity changes, respectively.

$$\begin{cases} \nabla P_G = \rho_l g \\ \mathbf{F}_{P_G} = -V_b\nabla P_G \\ \mathbf{F}_{P_D} = -V_b\nabla P_D \end{cases} \quad (7)$$

$$\mathbf{F}_P = \mathbf{F}_{P_G} + \mathbf{F}_{P_D} \quad (8)$$

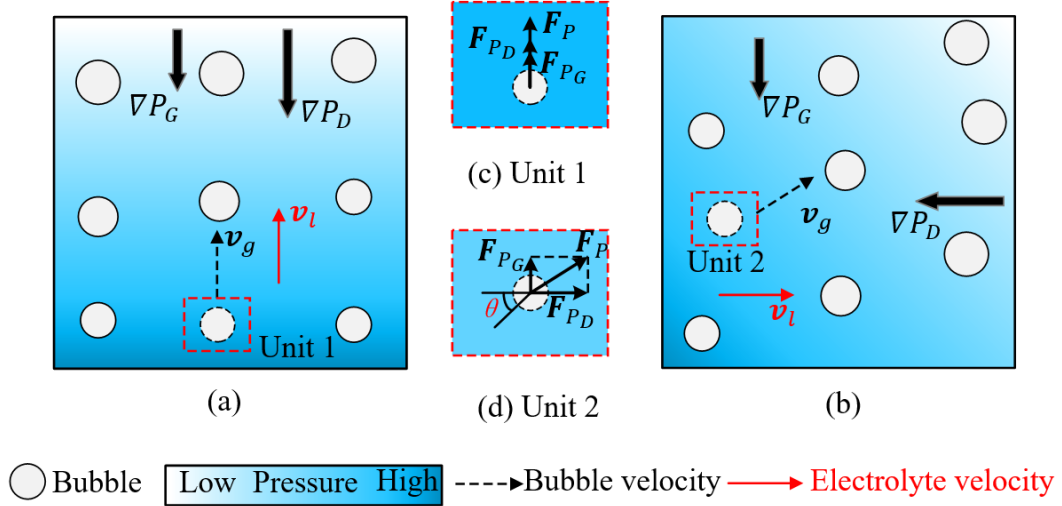


Fig. 3 Diagram of pressure gradient: (a) vertical flow, (b) horizontal flow, (c) pressure gradient

force on bubbles in unit 1, (d) pressure gradient force on bubbles in unit 2.

The direction of F_{P_G} is consistent with the direction of the electrolyte velocity in the vertical flow mode, but is perpendicular to the electrolyte velocity in the horizontal flow mode. Thus, the direction of F_P acting on the bubbles is the same as v_l in the vertical flow (Fig. 3(c)), whereas there is a certain angle θ between them in the horizontal flow (Fig. 3(d)).

The force due to gravity F_G can be calculated as follows:

$$F_G = \rho_g V_b g \quad (9)$$

where g is the acceleration of gravity, 9.8 m/s^2 , and $\rho_l \gg \rho_g$.

$$|F_{P_G}| \gg |F_G| \quad (10)$$

In fact, $|F_{P_G}|$ is about 10^4 times larger than $|F_G|$, and thus has a great influence on the bubbles.

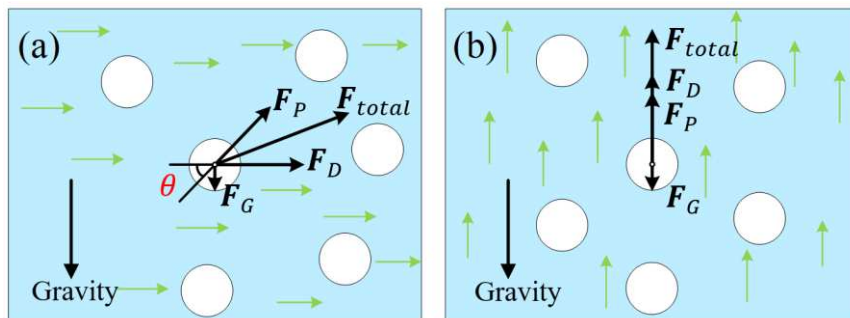


Fig. 4 Analysis of force: (a) horizontal flow, (b) vertical flow.

Combining Eqs. (1)–(3), the direction of the total force is different from that of the electrolyte velocity in horizontal flow (Fig. 4(a)). When the electrolyte flows vertically, the magnitude of \mathbf{F}_{total} is greater and the direction is consistent with the flow direction (Fig. 4(b)), and so the velocity of the bubble increases, the gas void fraction β decreases along the flow direction.

3. Multi-physical field models

ECM is an interdisciplinary subject covering mass transfer, energy transfer, momentum transfer, and chemical reactions[25]. By-products in the machining gap include sludge and hydrogen (Fig. 2). Due to the small ratio of sludge, its influence is neglected in this study[26]. The theoretical models of these multi-physical fields are established in this chapter.

3.1 Simulation model

To analyze the gas void fraction and the temperature along the flow path of blade ECM, the final machining time is modeled for the middle section of the blade body, and multi-physical field simulations are carried out. The structure of the flow channel on both sides is the same, the width and length of the flow channel are 0.5 mm and 40 mm, respectively, the height and length of the inlet are 2.5 mm and 6.5 mm, respectively, and the width of the outlet is 3 mm (Fig. 5). The parameters used in the simulations are given in Table 1.

Table 1 Simulation parameters

Parameter	Value
Initial electrolyte conductance k_0	14.6 S/m
Initial temperature T_0	302.65 K
Inlet electrolyte pressure P_0	0.5 MPa

Outlet electrolyte pressure P_1	0.1 MPa
Machining voltage U	18 V

The simulation model of blade ECM is illustrated in Fig. 5. The boundaries consist of an anode workpiece (boundaries 2–6) and cathode tools (boundaries 8, 9, 11, 12), with electrolyte flows through the inter-electrode gap from the two inlets (boundaries 1, 7) to the outlet (boundary 10). To simplify the proposed model, the following assumptions are made:

- 1) A bubble-flow model is used to simulate the gas–liquid two-phase flow.
- 2) The diffusion coefficient of the bubbles is independent of temperature, and has a constant value of $3.0 \times 10^{-6} \text{ m}^2/\text{s}$ [12].
- 3) Only Joule heat is considered as the heat source in ECM.

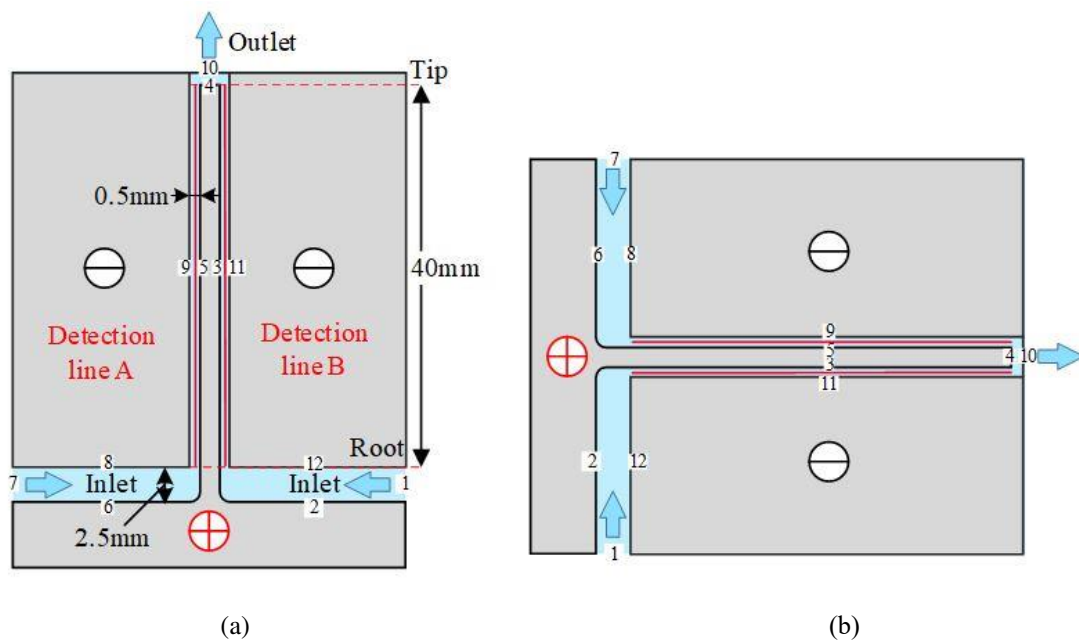


Fig. 5 Simulation model of blade ECM: (a) vertical flow, (b) horizontal flow.

3.2 Fluid field

Using the flow channel shown in Fig. 5, the flow field can be considered as a gas–liquid mixing flow, the density ρ and the dynamic viscosity μ satisfy the following relationships [27]:

$$\begin{cases} \rho = \beta\rho_g + (1 - \beta)\rho_l \\ \mu = \beta\mu_g + (1 - \beta)\mu_l \end{cases} \quad (11)$$

The flow state of the electrolyte is turbulent, and the electrolyte flow can be considered as an incompressible viscous flow, as described by the Navier–Stokes equations [12]:

$$\begin{cases} \nabla \cdot \mathbf{v}_l = 0 \\ -\mu\nabla^2 \mathbf{v}_l + \rho(\mathbf{v}_l \cdot \nabla)\mathbf{v}_l + \nabla P = 0 \end{cases} \quad (12)$$

where P is the pressure of the electrolyte.

The boundary conditions are given as follows:

$$\begin{aligned} P|_{\Gamma_{1,7}} &= P_0 \\ P|_{\Gamma_{10}} &= P_1 \end{aligned} \quad (13)$$

The electrode–electrolyte interfaces are subject to a no-slip condition:

$$\mathbf{v}|_{\Gamma_{2,3,4,5,6,8,9,11,12}} = 0 \quad (14)$$

3.3 Electric field

Based on theoretical analysis of the equilibrium state in the ECM process, the electric field parameters do not change with time. The distribution of the electric field potential ϕ obeys Laplace's equation:

$$\nabla^2 \phi = 0 \quad (15)$$

The electric field intensity \mathbf{E} in the electric field is equal to the negative value of the potential gradient:

$$\mathbf{E} = -\frac{d\phi}{dn} \mathbf{n} \quad (16)$$

The current density \mathbf{i} in the process of ECM is expressed as follows:

$$\mathbf{i} = \kappa \mathbf{E} \quad (17)$$

The electrolyte conductance is mainly affected by heat and bubbles. The relation between the electrolyte conductance κ , temperature T , and gas void fraction β in the simulations is described as follows [28]:

$$\kappa(x) = \kappa_0[(1 + \xi(T(x) - T_0))[1 - \beta(x)]^{bp}] \quad (18)$$

where κ_0 is the initial electrolyte conductance, T_0 is the initial temperature, i is the current density, and ξ , bp are the temperature coefficient and bubble ratio coefficient, respectively, selected as 0.021 and 1.5 based on processing experience. x is the flow path, and β can be obtained as follows:

$$\beta = \frac{Q_g}{Q} = \frac{Q_g}{Q_g + Q_l} \quad (19)$$

where Q_g is the volume flux of gas, Q_l is the volume flux of liquid, and Q is the total volume flux of the gas–liquid phases.

The boundary conditions are given as follows:

$$\varphi|_{\Gamma_{2,3,4,5,6}} = U \quad (20)$$

$$\varphi|_{\Gamma_{8,9,11,12}} = 0 \quad (21)$$

$$\frac{\partial \varphi}{\partial n}|_{\Gamma_{1,7,10}} \approx 0 \quad (22)$$

3.4 Reactant transport

The transport of reactants in the process of ECM is mainly driven by migration, convection, and diffusion. Diffusion is the main transport mechanism of reactants via the inter-electrode gap. Convection plays a major role in the transport of reactants in electrolyte adjacent to the anode surface. The governing equations are based on Fick's law, and the diffusion and convection forced by fluid flow can be described as follows [15]:

$$\frac{\partial C_j}{\partial t} + \nabla \cdot (C_j v_l - D_j \nabla C_j + D_j N_j) = 0 \quad (23)$$

where C_j (mol/m³) denotes the concentration of diluted species j , D_j is the diffusion coefficient, and N_j denotes the flux of diluted species j .

During the processing, metal ions are dissolved from the anode and hydrogen is produced near the cathode surface.



The boundary conditions are given as follows:

Hydrogen produced near the cathode surface $\Gamma_{8,9,11,12}$:

$$N_{H_2} = \frac{i}{2F} \quad (25)$$

Outlet:

$$\frac{\partial C_{H^2}}{\partial n} \Big|_{\Gamma_{10}} = 0 \quad (26)$$

Initial concentration:

$$C_{H^2} = 0 \quad (27)$$

where F is Faraday's constant, 96485 C/mol.

3.5 Thermal model

Heat is generated by electrode reactions and Joule heating in the electrolyte. The law of internal energy balance is given by [29]:

$$\rho_p C_p \frac{\partial T}{\partial t} + \rho_p C_p v_l \nabla T = \nabla \cdot (\lambda \nabla T) + P_{bulk} \quad (28)$$

$$\begin{cases} \omega_g = \frac{m_g}{m_g + m_l} = \frac{\rho_g Q_g}{\rho_g Q_g + \rho_l Q_l} \\ C_p = (1 - \omega_g) C_l + \omega_g C_g \approx C_l \\ \rho_p = \frac{m_g + m_l}{Q_g + Q_l} \approx \frac{\rho_l Q_l}{Q_g + Q_l} = \rho_l (1 - \beta) \end{cases} \quad (29)$$

where ω_g is the mass fraction of hydrogen, m_g is the gas mass flux, m_l is the liquid mass flux, C_p is the electrolyte specific heat capacity, and λ is the electrolyte thermal conductivity (0.6 W/m in this case). P_{bulk} is the Joule heating generated in the bulk of the electrolyte, which can be obtained by Joule's law as [30]:

$$P_{bulk} = iE \quad (30)$$

Based on the flow field characteristics in ECM, internal forced convection heat transfer was used in the simulation. The flow state of the electrolyte is turbulent, $Re > 2500$, then the thermal transfer coefficient h between the electrolyte and the electrode surface can be obtained as follows:

$$h = \frac{\lambda}{D} 0.023 Re^{0.8} Pr^{0.3} \quad (31)$$

$$Re = \frac{v_l D}{\nu} \quad (32)$$

Where D is the hydraulic diameter of the gap (about 1mm), Re is the Reynolds number, Pr is the Prandtl number, v_l and ν are the electrolyte flow velocity and kinematic viscosity coefficient respectively.

As metal materials, the electrode and workpiece have different thermal conductivities from that of the electrolyte. Therefore, the interfaces between the electrolyte and electrodes can be considered as outer boundaries. The boundary conditions are:

$$T|_{\Gamma_{1,2,3,4,5,6,7,8,9,11,12}} = T_0 \quad (33)$$

At the outlet:

$$\frac{\partial T}{\partial n}|_{\Gamma_{10}} = 0 \quad (34)$$

4. Simulation results

Using the multi-physical field models established in the previous section, the distribution of the gas void fraction and temperature can be simulated in the two different flow modes. To analyze the simulation results, two detection lines (A and B) are considered, both located at the middle of the flow channel (Fig. 5). The data on the detection lines and the distribution cloud of the gas void fraction and the temperature are obtained. Based on the changes in these variables obtained by the simulations, the conductance can be calculated.

4.1 Analysis of gas void fraction

According to the simulation results, the trend in the gas void fraction along the flow direction in the two different flow modes is similar. The cloud of the vertical flow is shown in Fig. 6(a). Bubbles are generated from the cathode surface, and the gas void fraction near the cathode surface is relatively high. The data distribution along the detection lines (A and B) is similar. At the blade root, the gas void fraction is 0 in both flow modes. The gas void fraction increases by 31.8% from the blade root to the tip when the electrolyte flows horizontally in ECM. By comparison, the gas void fraction of the vertical flow increases by 29.4% (Fig. 6(b)).

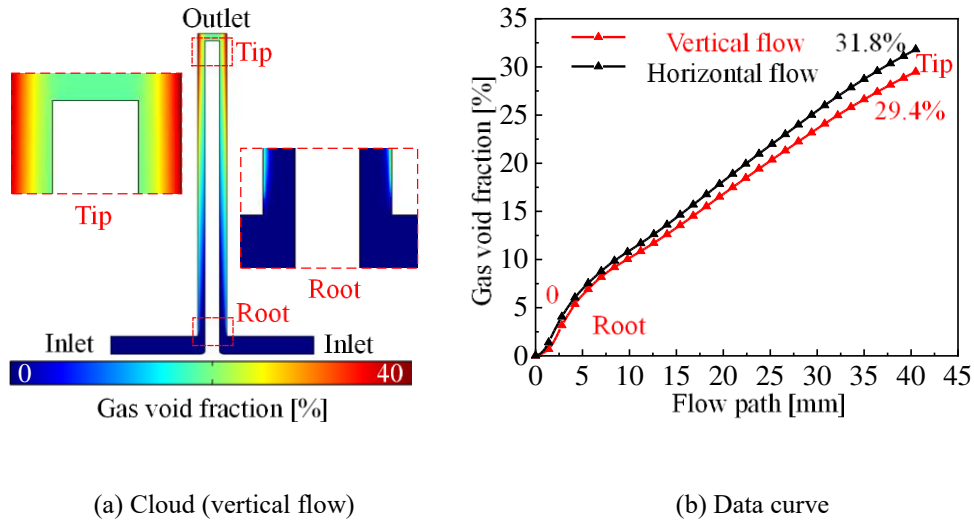


Fig. 6 Gas void fraction distribution.

Assuming that the mass of the two gas–liquid phases is conserved and there is no mass conversion, the mass continuity equation of the gas phase is as follows:

$$\frac{d(\rho_g \beta A v_g)}{dx} = \eta_g k_g i \quad (35)$$

where A is the area of the cross-section of the flow channel. The gas void fraction is inversely proportional to the velocity of the bubbles. Thus, the gas void fraction decreases as the bubble velocity increases. Compared with the horizontal flow, the velocity of bubbles is higher in the vertical flow, and the gas void fraction decreases accordingly. Hence, the gas void fraction at the tip in vertical flow is 2.4% lower than that in horizontal flow (Fig. 6(b)).

4.2 Analysis of temperature

The changes of temperature are similar to those of the gas void fraction (Fig. 7(a)). The initial temperature at the blade root is 302.65 K in both flow modes. As heat accumulates along the flow direction, the temperature increases by 15.8 K in horizontal flow mode and by 15.2 K in the vertical flow (Fig. 7(b)).

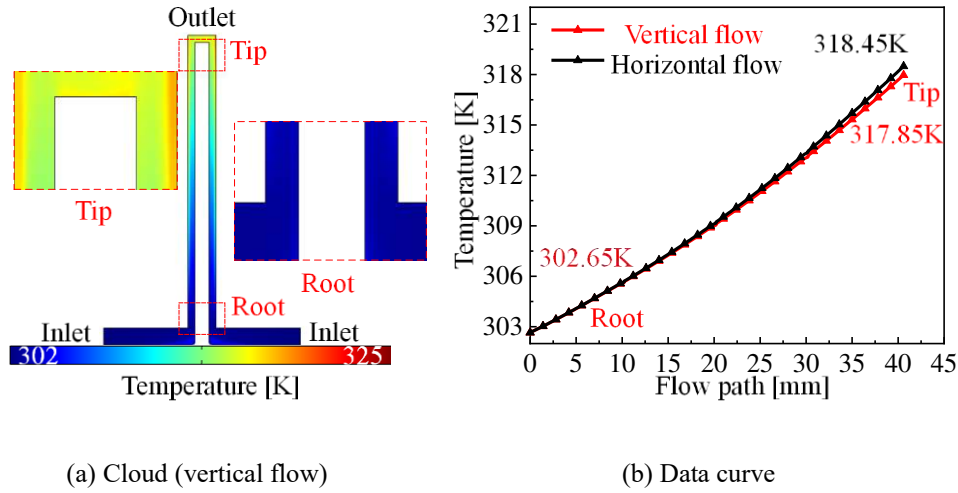


Fig. 7 Temperature distribution.

Based on Eqs. (28) and (29), the temperature distribution in ECM is affected by the electrolyte velocity and gas void fraction, the temperature is proportional to the gas void fraction. In the cloud, the temperature is higher near the cathode surface because of the high gas void fraction. Compared with the horizontal flow, the gas void fraction in vertical flow is lower and the temperature decreases accordingly. Therefore, the temperature of the electrolyte is 0.6 K lower at the tip in vertical flow than in horizontal flow.

4.3 Calculation and analysis of conductance

In ECM, the conductance changes along the direction of electrolyte flow with variations in the gas void fraction and the temperature. The distribution of the conductance κ can be calculated by Eq. (18). The conductance decreases gradually along the flow direction (Fig. 8).

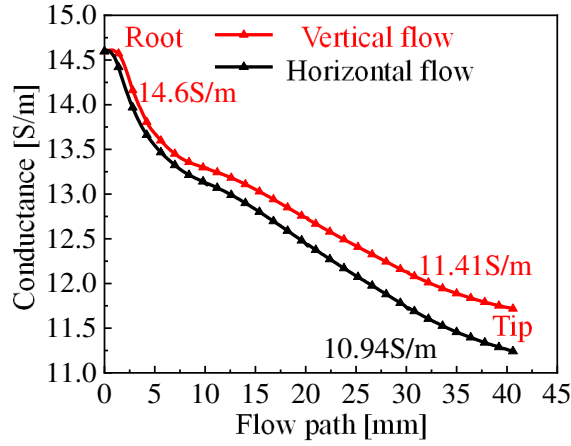


Fig. 8 Distribution of conductance.

The initial value of electrolyte conductance is 14.6 S/m at the root. This decreases by 3.19 S/m in vertical flow and by 3.66 S/m in horizontal flow. This difference occurs because, in vertical flow, the growth rate of both the gas void fraction and temperature are reduced, and conductance that is more uniform is thus achieved. Therefore, the conductance at the blade tip in vertical flow is 0.47 S/m higher than that in horizontal flow. When the processing is in a stable state, the relationship between the machining gap Δ_b and conductance κ can be expressed as follows:

$$\Delta_b(x) = \eta \omega \frac{U_R \kappa(x)}{v_c} \quad (36)$$

where η is the current efficiency, ω is the volume electrochemical equivalent, v_c is the feed speed of the tool, and U_R is the voltage. The uniformity of the machining gap along the flow direction will be improved in vertical flow, thus enhancing the machining accuracy and surface quality.

5. Experimental results

5.1 Experiments

To verify the accuracy of the simulations, experiments were carried out using a vertical electrolyte flow, and the experimental conditions are listed in Table 2.

Table 2 Experimental conditions

Condition	Value

Workpiece material	Inconel 718
Cathode material	304 stainless steel
Electrolyte	NaNO ₃ solution
Electrolyte temperature	302.65 K
Feeding velocity	0.5 mm/min
Feeding distance	9.76 mm
Voltage	18 V DC

The experimental system used for blade ECM in this study is shown in Fig. 9(a). It mainly includes fixture, two feed shafts, two cathodes and a workpiece. The geometric design method of the cathode is the common $\cos\theta$ method[31]. Neutral NaNO₃ solution is used due to its passivating properties to obtain high-quality products[32]. The fixture is composed of front and back parts, made of epoxy. The machine tool controls the cathodes through the feed shafts, the cathodes are inserted into the fixture along the feed channels on both sides, feed to each other at a constant speed. The electrolyte flows in from the inlet on both sides of the bottom and flows out from the outlet on the top. Electrolyte fills the inter-electrode gap and flows vertically from root to tip, the direction of gravity is opposite to the electrolyte flow direction.

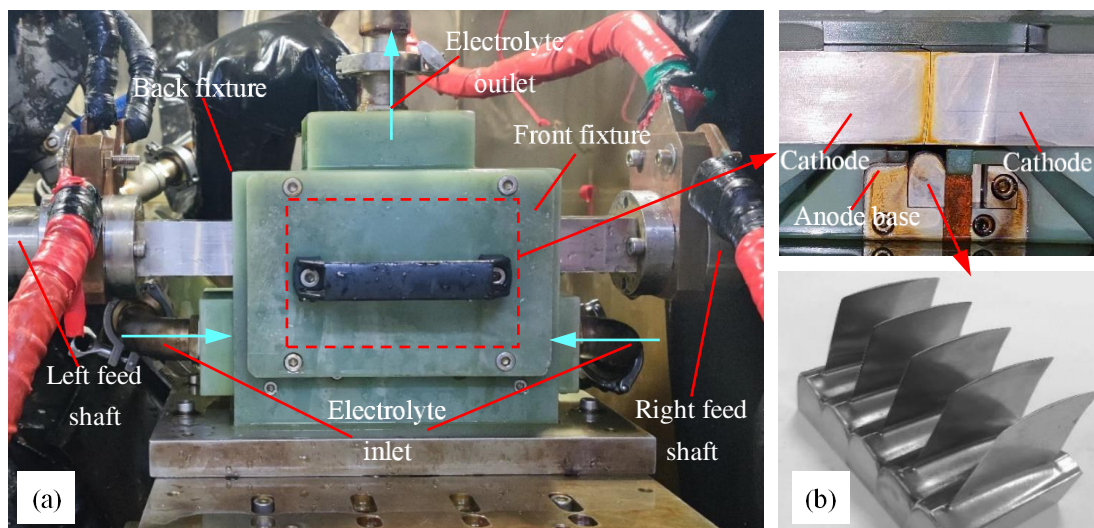


Fig. 9 Experimental system for the ECM of the blade: (a) fixture (b) specimens machined by ECM.

In the experiments, the machining time was 19.5 min, the current changed smoothly, and no

abnormal short-circuit sparks occurred during the machining process. The machined blades obtained from five processing experiments were shown in Fig. 9(b).

5.2 Machining deviation

The machined blades were measured along the line C on the middle section of the blade body (Fig. 10(a)) by a coordinate measuring machine. The edge profile of the machined edges was obtained, and a comparison of the machined edge profile with the standard profile allowed us to calculate the machining deviation of the line C (shown in Fig. 10(b)).

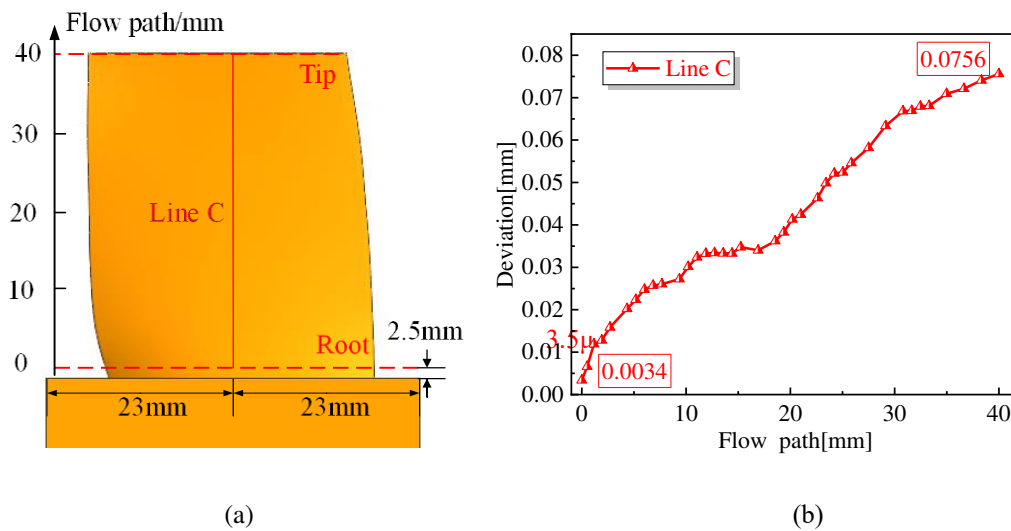


Fig. 10 (a) Schematic diagram of measurement, (b) deviation distribution.

It can be seen that the edge profile of the blade manufactured by ECM exhibits a positive deviation that gradually increases along the flow direction. The machining deviation changes from 3.4 μm (blade root) to 75.6 μm (blade tip) on the line C. The difference in the deviation at the root and tip is 72.2 μm .

According to the simulation results, the gas void fraction and the temperature change along the flow direction in such a way that the conductivity of the electrolyte decreases. Hence, by Faraday's law, the current density and the material removal rate decrease along the flow direction. Thus, the variation observed in the experiments is consistent with the simulation results.

5.3 Surface quality

The surface quality is quantified by the surface roughness R_a of the machined surface. We selected two rectangular areas (1, 2) and ten lines (D_{1-5} , E_{1-5}) near the root and tip of the blade, as shown in Fig. 11. The Keyence 3D profile measuring instrument and scanning electron microscopy (SEM, HITACHI Regulus 8220) were used to observe the surface topography, and a Taylor–Hobson profiler was used to obtain the line roughness along the lines.

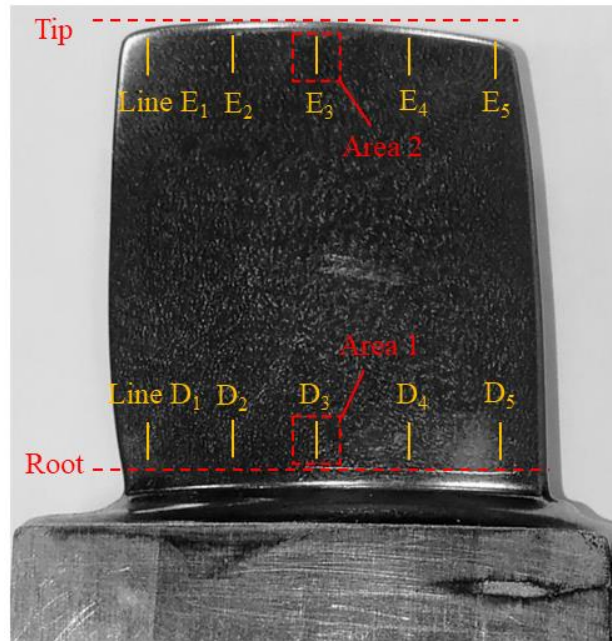


Fig. 11 Observation areas and sampling lines on the machined blade.

The surface topography and surface roughness measurement results are shown in Fig. 12 and 13. The black dots in the area 1 and area 2 are electrochemical pitting generated by the non-uniform corrosion of the materials, as shown in Fig. 12, similar conclusions were also reported by Wang J et. al[33]. It can be observed that the smoothness is better in the area 1, near the root of the machined blade.

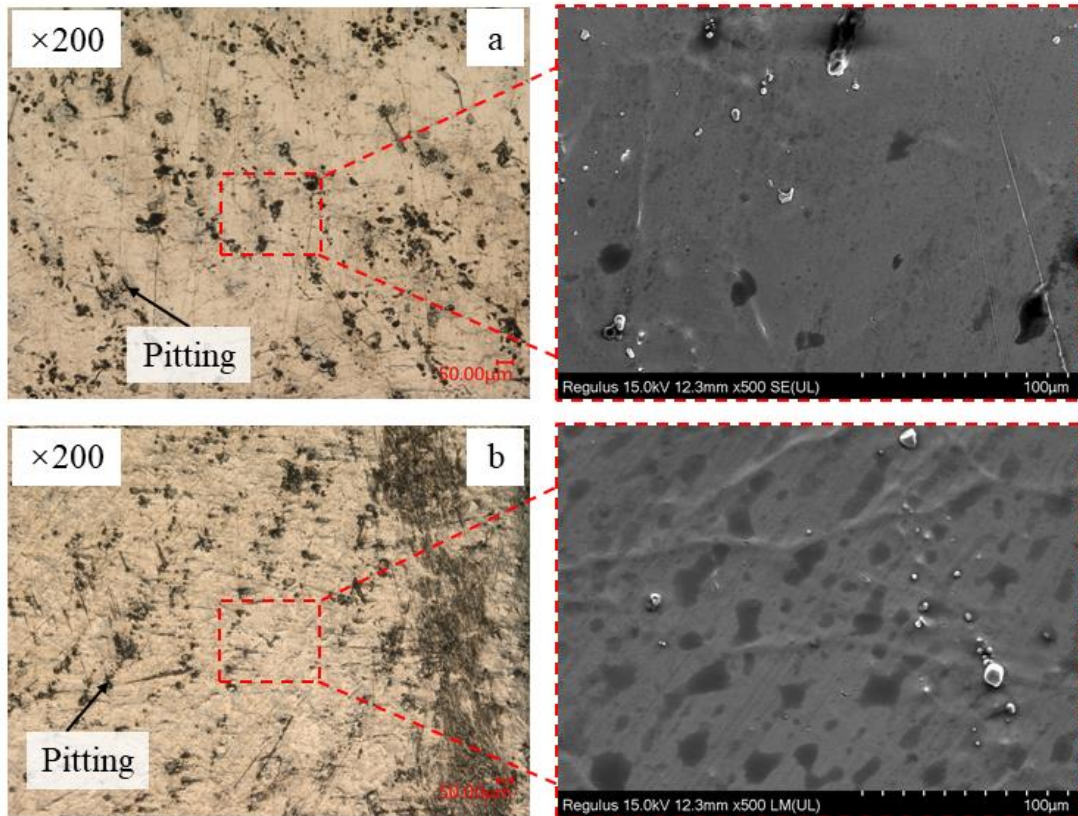


Fig. 12 Surface topography of the (a) area 1 and (b) area 2.

The surface roughness R_a along the lines $D_{1\sim5}$ and $E_{1\sim5}$ were shown in Fig. 13 (a) and (b) respectively. The surface roughness R_a near the root and tip varied from $0.193\ \mu\text{m}$ to $0.248\ \mu\text{m}$ and $0.282\ \mu\text{m}$ to $0.348\ \mu\text{m}$, respectively. The average surface roughness of the machined blade near the root is $R_a=0.222\ \mu\text{m}$, which is $R_a=0.315\ \mu\text{m}$ near the tip, as shown in Fig. 14. The average surface roughness increases along the flow direction, and the difference over the flow path is about $0.1\ \mu\text{m}$.

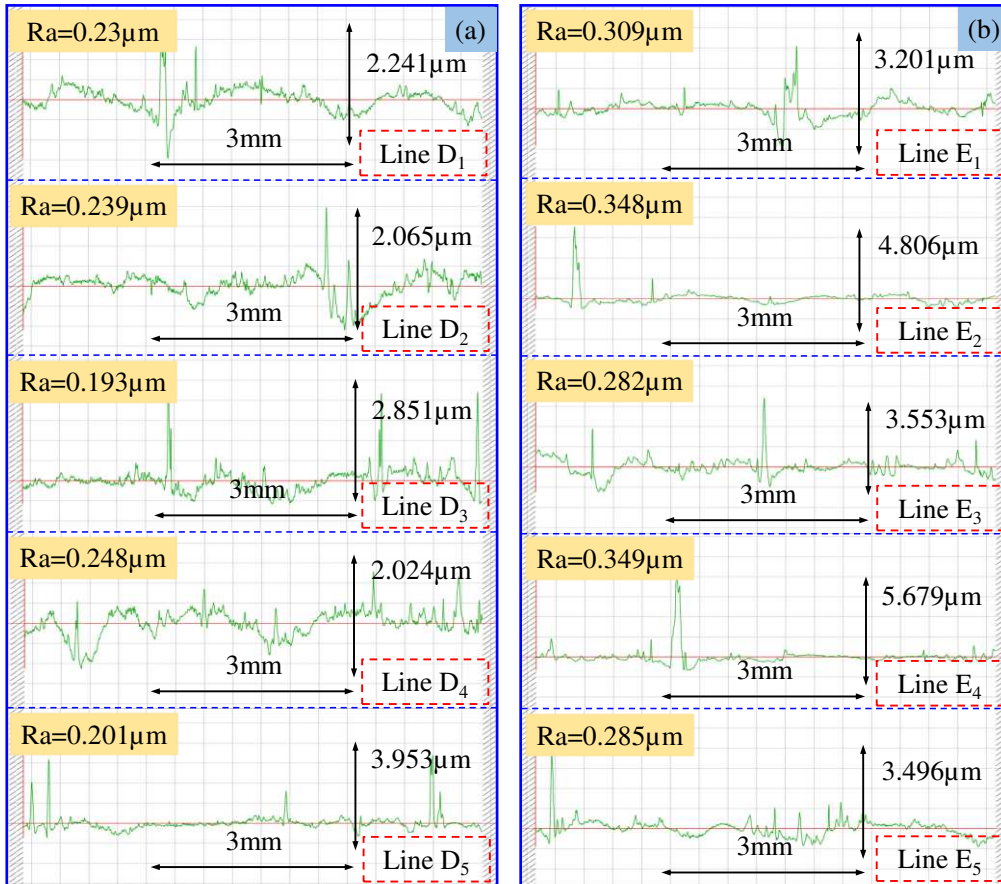


Fig. 13 Surface roughness of the lines (a) D₁₋₅ and (b) E₁₋₅

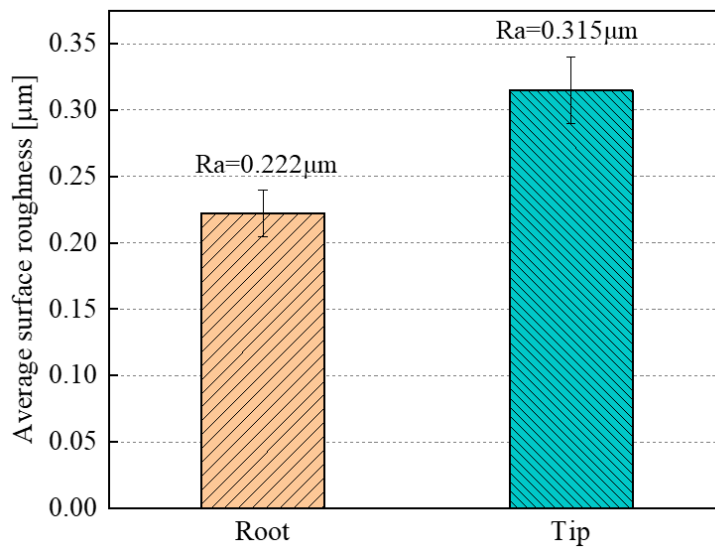


Fig. 14 Average surface roughness of the machined blade

In ECM, the current density affects the surface quality. The high potential gradient in the solution preferentially dissolves the metal at sites with higher values of the surface roughness, resulting in a

smooth surface. According to the simulation results, the gas void fraction increases along the flow direction. As the surface quality decreases as the current density decreases, the surface quality of the root is better than that of the tip, which is consistent with the experimental results.

Based on the analysis of the experimental results of the machining deviation and surface quality, the validity and correctness of the simulations were verified. The experimental results show that the machining quality can be improved by reducing the gas void fraction, the machining deviation ranged from $3.4\ \mu\text{m}$ to $75.6\ \mu\text{m}$ and surface roughness values of $R_a < 0.35\ \mu\text{m}$ can be obtained by using a vertical electrolyte flow.

6. Conclusion

1) The bubble dynamics analysis were conducted considering the influence of gravity, and a vertical flow mode for blade ECM has been proposed. The vertical flow mode can effectively increase the bubble velocity and reduce the gas void fraction.

2) A multi-physical field theoretical model was established to simulate the equilibrium state of blade ECM in the two flow modes. Compared with the horizontal flow, the vertical flow reduced the gas void fraction and the temperature at the outlet by 2.4% and 0.59 K, respectively, leading to an improvement of 0.47 S/m in conductance, which was useful for enhancing the machining quality.

3) Vertical flow experiments were carried out, after measuring the machined blade, the variation of the machining deviation and the surface quality along the flow path were obtained. The deviation gradually increased along the flow direction, changed from $3.4\ \mu\text{m}$ to $75.6\ \mu\text{m}$, and the difference in the magnitude of the deviation was $72.2\ \mu\text{m}$. The average surface roughness changed from $R_a=0.222\ \mu\text{m}$ to $R_a=0.315\ \mu\text{m}$, the surface quality was very well. The simulations and the experimental results were consistent, the validity and correctness of the simulations were verified.

Although the machining quality is improved and the flow state is better in vertical flow, due to the continuous generation of a large number of bubbles, there are certain changes in machining accuracy and surface quality along the flow path. To improve the consistency of machining accuracy along the flow path in vertical flow, further research on the pulsed machining will be carried out.

Declaration

Funding: This work was sponsored by the National Natural Science Foundation of China (91860135), the National Natural Science Foundation of China for Creative Research Groups (51921003) and the National Science and Technology Major Project (2017-VII-0004-0097).

Conflict of interest: The authors declare that they have no known competing financial interests or personal relationships that could have appeared to influence the work reported in this paper.

Availability of data and material: Not applicable.

Code availability: Not applicable.

Ethical approval: This paper is new. Neither the entire paper nor any part of its content has been published or has been accepted elsewhere. It is not being submitted to any other journal as well.

Consent to participate: Not applicable.

Consent to publication: Not applicable.

Author Contributions: All authors contributed to the study conception and design. Material preparation, data collection and analysis were performed by [Mingzhu Ren], [Dong Zhu] [Zhenhao Hou] and [Gaopan Lei]. The first draft of the manuscript was written by [Mingzhu Ren] and all authors commented on previous versions of the manuscript. All authors read and approved the final manuscript.

References

- [1] Hua J, Li ZY (2009) Cathode Design of Aero-Engine Blades in Electrochemical Machining Based on Characteristics of Gap Distribution. *Adv Mater Res*; 69-70: 248–252.
- [2] Zhu D, Zhu D, Xu ZY (2012) Optimal design of the sheet cathode using W-shaped electrolyte flow mode in ECM. *Int J Adv Manuf Technol* 62, 147–156.
- [3] Asokan P, Kumar RR, Jeyapaul R, Santhi M (2008) Development of multi-objective optimization models for electrochemical machining process. *Int J Adv Manuf Technol* 39:55–63
- [4] Qu NS, Xu ZY (2013) Improving machining accuracy of electrochemical machining blade by optimization of cathode feeding directions. *Int J Adv Manuf Technol* 68(5-8):1565–1572.
- [5] Rajurkar KP, Zhu D, McGeough JA, Kozak J, De Silva A (1999) New Developments in Electro-Chemical Machining. *CIRP Ann - Manuf Technol* 48(2): 567–79.
- [6] Geethapriyan T, Kalaichelvan K, Muthuramalingam T, et al. (2018) Performance analysis of process parameters on machining α - β titanium alloy in electrochemical micromachining process. *Proc IMechE Part B: J Engineering Manufacture* 232(9): 1577–1589.
- [7] Leese R, Ivanov A (2018) Electrochemical micromachining: review of factors affecting the process applicability in micro-manufacturing. *Proc IMechE Part B: J Engineering Manufacture* 232(2): 195–207.
- [8] XiaoChao Z., ChangYong C, HongXin W. et al. (2020) Study on the multi-field coupling model of electrolyte temperature distribution in electrochemical machining. *Int J Adv Manuf Technol* 109: 1655–1662.
- [9] Lei G, Zhu D, Zhu D. (2022) Research on multiphysics coupling fields in electrochemical trepanning of lateral flow. *Int J Adv Manuf Technol* 119: 5131–5141..
- [10] Klocke F, Zeis M, Harst S, et al (2013) Modeling and Simulation of the Electrochemical Machining (ECM) Material Removal Process for the Manufacture of Aero Engine Components. *Procedia CIRP* 8: 265–270.
- [11] Kozak J (2013) The Computer Simulation of Electrochemical Shaping Processes. *IAENG Transactions on Engineering Technologies*. Springer Dordrecht, pp 95-107.

- [12] Fujisawa T, Inaba K, Yamamoto M, et al (2008) Multiphysics Simulation of Electrochemical Machining Process for Three-Dimensional Compressor Blade. *ASME. J. Fluids Eng* 130(8): 081602.
- [13] Klocke F, Zeis M, Herrig T, et al (2014) Optical in Situ Measurements and Interdisciplinary Modeling of the Electrochemical Sinking Process of Inconel 718. *Procedia CIRP* 24: 114–119.
- [14] Klocke F, Zeis M, Klink A (2015) Interdisciplinary modelling of the electrochemical machining process for engine blades. *CIRP Ann - Manuf Technol* 64(1): 217–220.
- [15] Fang XL, Qu NS, Zhang YD, et al (2014) Effects of pulsating electrolyte flow in electrochemical machining. *J Mater Process Technol* 214(1): 36–43.
- [16] Wang W, Zhu D, Qu NS, et al (2010) Electrochemical drilling with vacuum extraction of electrolyte. *J Mater Process Technol* 210(2): 238–244.
- [17] Tang L, Feng X, Zhai KG, Ji Y, Wang Z, Lei QB, Ren L (2019) Gap flow field simulation and experiment of electrochemical machining special-shaped inner spiral tube. *Int J Adv Manuf Technol* 100: 2485-2493
- [18] Guo J, Zhu D, Yang Y(2021). Electrochemical machining with independent electrolyte supply at blade leading/trailing edge. *Int J Adv Manuf Technol* 114: 1119–1129.
- [19] Zhu D, Zhang RH, Liu C (2017) Flow field improvement by optimizing turning profile at electrolyte inlet in electrochemical machining. *Int J Precis Eng Manuf* 18(1): 15–22.
- [20] Zhu D, Zhu D, Xu ZY, et al (2010) Investigation on the flow field of W-shape electrolyte flow mode in electrochemical machining. *J Appl Electrochem* 40(3): 525–532.
- [21] Auton TR (1983) The dynamics of bubbles, drops and particles in motion in liquids. Dissertation, University of Cambridge, UK.
- [22] Delnoij E, Lammers FA, Kuipers JAM, et al (1997) Dynamic simulation of dispersed gas-liquid two-phase flow using a discrete bubble model. *Chem Eng Sci* 52(9): 1429–1458.
- [23] Odar F (1964) Forces on a sphere accelerating in a viscous fluid. *J Fluid Mech* 18(2): 302–314.
- [24] Clift R, Grace JR, Weber ME (1978) Bubbles, drops, and particles. Academic Press, New York, pp 22-28
- [25] McGeough JA (1974) Principles of electrochemical machining. London: Chapman & Hall.
- [26] Wang M H, Tong W J, Qiu G Z, et al (2019) Multiphysics study in air-shielding electrochemical micromachining. *J Mater Process Tech* 43:124-135.

- [27] Hu XY, Zhu D, Li JB, et al (2019) Flow field research on electrochemical machining with gas film insulation. *J Mater Process Tech* 267: 247-256.
- [28] Thorpe JF, Zerkle RD (1969) Analytic determination of the equilibrium electrode gap in electrochemical machining. *Int J Mach Tool Design Res* 9(2): 131–144.
- [29] Cengel, Yunus A (2003) *Heat Transfer: A Practical Approach*. 2nd ed. New York: McGraw-Hill.
- [30] Deconinck D, Damme SV, Deconinck J (2012) A temperature dependent multi-ion model for time accurate numerical simulation of the electrochemical machining process. Part I: Theoretical basis. *Electrochimica Acta* 60(8): 321–328.
- [31] Tipton H (1968) The determination of tool shape for ECM. *Machinery and Production Engineering* 2: 325-328.
- [32] D Wang, Zhu Z, He B, et al (2017) Effect of the breakdown time of a passive film on the electrochemical machining of rotating cylindrical electrode in NaNO_3 solution. *J Mater Process Tech* 239:251–257.
- [33] Wang J, Xu Z, Wang J, et al (2021) Anodic dissolution characteristics of Inconel 718 in $\text{C}_6\text{H}_5\text{K}_3\text{O}_7$ and NaNO_3 solutions by pulse electrochemical machining. *Corrosion Science* 183: 109335.